

# An implicit ODE-based numerical solver for the simulation of the Heisenberg-Euler equations in 3+1 dimensions

Arnau Pons Domenech<sup>a,b</sup>, Hartmut Ruhl<sup>a</sup>

<sup>a</sup>*Ludwig-Maximilians-Universität München  
Theresienstr.37, 80333 München, Germany*

<sup>b</sup>*Max-Planck-Institut für Quantenoptik  
Hans-Kopfermann-Str.1, 85748 Garching, Germany*

---

## Abstract

With the advent of ultra-high power lasers the nonlinear nature of the vacuum of quantum electrodynamics (QED) can be probed. Due to the highly nonlinear structure of the underlying equations new numerical algorithms are required. A numerical scheme for simulating the nonlinear optical effects of the QED vacuum in up to 3 spatial dimensions plus time is derived. Its properties are discussed. The validity of the numerical approach is verified with the help of known analytic results. The algorithm is used to explore nonlinear all optical effects of the nonlinear vacuum for which analytic methods are inefficient or impossible.

*Keywords:* Heisenberg-Euler, Nonlinear optical vacuum effects, Polarisation, Birefringence, Harmonics

*2016 MSC:*

---

## 1. Introduction

It has long been suspected that the structure of the QED vacuum can lead to nonlinear polarization and magnetization terms in the vacuum wave equations for electromagnetic (em)-fields. First derived by Heisenberg and Euler [1] and later introduced into the QED framework by Schwinger [2] the breaking of the spatial isotropy of the vacuum by strong em-fields is expected to lead to many new effects such as vacuum birefringence [3], diffraction [4, 5], scattering [6], dispersion [7], reflection [8], the generation of higher harmonics [9, 10] and others. While the theory has long been known the theoretical investigation of these effects has started only recently. None of them has yet been measured. With the advent of Petawatt (PW)-class lasers (e.g. ELI-NP and others [11,

---

*Email addresses:* [arnau.pons@physik.uni-muenchen.de](mailto:arnau.pons@physik.uni-muenchen.de) (Arnau Pons Domenech),  
[hartmut.ruhl@physik.uni-muenchen.de](mailto:hartmut.ruhl@physik.uni-muenchen.de) (Hartmut Ruhl)

12, 13]) it is expected that some of the nonlinear vacuum effects might become accessible experimentally in the near future.

While there are by now many analytical endeavors to compute nonlinear vacuum effects [9, 10, 14, 15, 16] there are only a few on the numerical side [9]. Analytical calculations have many limitations such as low energies, the requirement of special pulse shapes and many more. They become highly complex when attempting to reproduce realistic experimental settings. Furthermore, the analytical theories can only consider light by light interaction while, e.g., plasma effects have to be neglected.

Thus, in the present paper a numerical algorithm is introduced that only makes use of a minimal set of assumptions and has the power to augment analytical investigations. With the numerical approach presented in this paper it is possible to explore almost all nonlinear effects of the quantum vacuum simultaneously and not in isolation and for any given setting. The algorithm is efficient and accurate and can be used in up to three spatial dimensions plus time (3+1). While the algorithm in [9] works in 1+1 the extension to 3+1 is nontrivial as is shown in section 4.

The paper is divided into 8 sections. In section 2 the Heisenberg-Euler Lagrangian and its weak-field expansion are introduced. The weak-field expansion is then used in section 3 to derive a modified set of Maxwell equations, that account for light by light scattering. In section 4 the derivation of the numerical algorithm based on the Heisenberg-Euler (HE) equations in weak-field expansion is derived. In section 5 the properties of the numerical algorithm are discussed. In section 6 the most prominent nonlinear QED vacuum effects are reviewed [9, 14, 15] and in section 7 they are benchmarked with simulations based on the numerical algorithm derived in the present paper. Section 9 contains a summary of results and their significance. Finally in section 10 an outlook into possible future applications of the numerical algorithm is given.

## 2. Heisenberg-Euler Lagrangian

It is useful to normalize the electromagnetic invariants  $\mathcal{F}, \mathcal{G}$  and secular invariants  $a, b$  to the critical field strength given by  $E_{cr} = m^2 c^3 / e \hbar = 1.3 \times 10^{18} \text{V/m}$  [1] leading to

$$\mathcal{F} = -\frac{F^{\mu\nu} F_{\mu\nu}}{4E_{cr}^2} = \frac{1}{2E_{cr}^2} \left( \vec{B}^2 - \frac{\vec{E}^2}{c^2} \right), \quad \mathcal{G} = -\frac{F^{\mu\nu} F_{\mu\nu}^*}{4E_{cr}^2} = \frac{\vec{E} \cdot \vec{B}}{c E_{cr}^2}, \quad (1)$$

$$a = \sqrt{\sqrt{\mathcal{F}^2 + \mathcal{G}^2} + \mathcal{F}}, \quad b = \sqrt{\sqrt{\mathcal{F}^2 + \mathcal{G}^2} - \mathcal{F}}, \quad (2)$$

where  $F$  is the electromagnetic tensor and  $F^*$  its dual. Using these definitions the effective HE-Lagrangian representing the interaction of a constant electromagnetic field with virtual electron-positron pairs is given by [2]

$$\mathcal{L}_{HE} = -\frac{m^4}{8\pi^2} \int_0^\infty ds \frac{e^{-s}}{s^3} \left( \frac{s^2}{3} (a^2 - b^2) - 1 + abs^2 \cot(as) \coth(bs) \right). \quad (3)$$

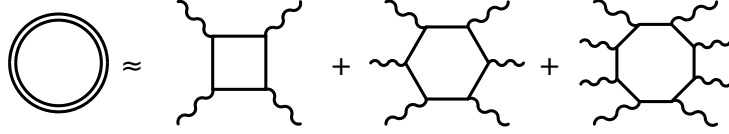


Figure 1: Depiction of the weak-field expansion of the HE-Lagrangian using Feynman diagrams. To the left the full seeded loop and on the right the 4, 6 and 8 photon box diagrams are shown. Note that these correspond to (4a), (4b), and (4c) respectively.

It has been shown both numerically [17] and analytically [18] that the approximation of a constant background em-field holds when the variations of the field strength are on a much larger scale than the Compton wavelength  $\lambda_C = \frac{\hbar}{m_e c} = 2.426 \times 10^{-12} \text{m}$  [19].

The evaluation of the integral in (3) is challenging. However, since the critical field is assumed to be much larger than all other em-fields involved a weak-field approximation, i.e., a Taylor series of the cot and coth functions for small  $a$  and  $b$  is made. This yields the following weak field approximation of the HE-Lagrangian

$$\mathcal{L}_{HE} \approx \frac{m^4}{360\pi^2} (4\mathcal{F}^2 + 7\mathcal{G}^2) \quad (4a)$$

$$+ \frac{m^4}{630\pi^2} (8\mathcal{F}^3 + 13\mathcal{F}\mathcal{G}^2) \quad (4b)$$

$$+ \frac{m^4}{945\pi^2} (48\mathcal{F}^4 + 88\mathcal{F}^2\mathcal{G}^2 + 19\mathcal{G}^4) \quad (4c)$$

$$+ \frac{4m^4}{1485\pi^2} (160\mathcal{F}^5 + 332\mathcal{F}^3\mathcal{G}^2 + 127\mathcal{F}\mathcal{G}^4). \quad (4d)$$

Three things are worth noting: Firstly, (3) and (4) only depend on  $\mathcal{F}$  and  $\mathcal{G}$ . Secondly, due to the definition of the electromagnetic invariants in (1)  $\mathcal{F}, \mathcal{G} \sim (E/E_{cr})^2$  holds. Therefore the term (4a) is  $\mathcal{O}((E/E_{cr})^4)$ , term (4b)  $\mathcal{O}((E/E_{cr})^6)$  and so on. This implies that in the weak-field regime,  $E < E_{cr}$ , the higher order terms become negligible. The expansion in (4) corresponds to processes with 4, 6, 8 and 10 photons contributing to the closed loop as shown in figure 1. Furthermore, computing the probability for pair production in a constant electric field using the full HE-Lagrangian [2]

$$R_{e^+ e^-} = \frac{\alpha E^2}{4\pi^3} \sum_{n=1}^{\infty} \frac{1}{n^2} e^{-n\pi \frac{E_{cr}}{E}}. \quad (5)$$

shows that the production of real pairs is exponentially suppressed.

### 3. Modified Maxwell equations

For simplicity we use natural units  $\hbar = c = 1$  combined with Lorentz-Heaviside units  $e^2 = 4\pi\alpha$ . In these units the vacuum Maxwell-Lagrangian is

given by

$$\mathcal{L}_{MW} = -\frac{F^{\mu\nu}F_{\mu\nu}}{4} \xrightarrow{E \rightarrow \frac{E}{c\epsilon_r}} -\frac{m^4}{4\pi\alpha} \frac{F^{\mu\nu}F_{\mu\nu}}{4}. \quad (6)$$

The Maxwell-Lagrangian combined with the HE-Lagrangian yields the Lagrangian for the propagation of light in vacuum  $\mathcal{L} = \mathcal{L}_{MW} + \mathcal{L}_{HE}$ . Making use of the Lagrange equations of the second kind and the cartesian representation of the electromagnetic tensor results in

$$\partial_t \left( \vec{E} + \mu \frac{\partial \mathcal{L}_{HE}}{\partial \vec{E}} \right) = \nabla \times \left( \vec{B} - \mu \frac{\partial \mathcal{L}_{HE}}{\partial \vec{B}} \right), \quad (7)$$

where  $\mu = 4\pi\alpha/m^4$ . With the help of (7) Maxwell's equations [20] become

$$\partial_t \vec{B} = -\nabla \times \vec{E}, \quad (8a)$$

$$\partial_t (\vec{E} + \vec{P}) = \nabla \times (\vec{B} - \vec{M}), \quad (8b)$$

where

$$\vec{P} = \mu \frac{\partial \mathcal{L}_{HE}}{\partial \vec{E}} \quad \text{and} \quad \vec{M} = \mu \frac{\partial \mathcal{L}_{HE}}{\partial \vec{B}}. \quad (9)$$

Equations (8a) and (8b) form a set of nonlinear dynamical equations for the em-fields. They will be solved numerically in the present paper.

## 4. Numerical Method

### 4.1. Linear case

The linear case is considered first. Assuming  $\vec{P} = \vec{M} = 0$  we find, e.g., for the curl of  $\vec{B}$  in (8b)

$$\begin{aligned} \nabla \times \begin{pmatrix} B_x \\ B_y \\ B_z \end{pmatrix} &= \begin{pmatrix} \partial_y B_z - \partial_z B_y \\ \partial_z B_x - \partial_x B_z \\ \partial_x B_y - \partial_y B_x \end{pmatrix} \\ &= \underbrace{\begin{pmatrix} 0 & 0 & 0 \\ 0 & 0 & -1 \\ 0 & 1 & 0 \end{pmatrix}}_{\mathbf{Q}_x} \partial_x \vec{B} + \underbrace{\begin{pmatrix} 0 & 0 & 1 \\ 0 & 0 & 0 \\ -1 & 0 & 0 \end{pmatrix}}_{\mathbf{Q}_y} \partial_y \vec{B} + \underbrace{\begin{pmatrix} 0 & -1 & 0 \\ 1 & 0 & 0 \\ 0 & 0 & 0 \end{pmatrix}}_{\mathbf{Q}_z} \partial_z \vec{B} \\ &= \sum_{i \in \{x,y,z\}} \mathbf{Q}_i \partial_i \vec{B}. \end{aligned} \quad (10)$$

where  $\mathbf{Q}_i = (\epsilon_{ijk})_{j,k} \in \mathbb{R}^{3 \times 3}$  implying that equations (8) can be written as

$$\partial_t \vec{f} = \sum_{i \in \{x,y,z\}} \begin{pmatrix} 0 & \mathbf{Q}_i \\ -\mathbf{Q}_i & 0 \end{pmatrix} \partial_i \vec{f}, \quad (11)$$

where  $\vec{f} = (\vec{E}, \vec{B})^T \in \mathbb{R}^6$ .

In order to convert (11) into a finite set of ordinary differential equations (ODEs) the derivatives in space are replaced by a finite difference scheme. To do this a grid of  $N = N_x \cdot N_y \cdot N_z$  equally spaced points  $\mathcal{B} = \{x_{a,b,c} = (a\Delta_x, b\Delta_y, c\Delta_z)\} \subset \mathbb{R}^3$  is introduced and the vector  $\vec{f}$  of the em-field at the grid points  $\vec{f}_{a,b,c} = \vec{f}(x_{a,b,c})$  is merged into a new vector  $\vec{F} \in \mathbb{R}^{6N}$ , such that  $(\vec{f}_{a,b,c})_l = F_{\mathcal{I}(a,b,c)+l}$ . Here  $\mathcal{I} : [0, N_x] \times [0, N_y] \times [0, N_z] \rightarrow [0, 6N]$  is a bijection, which assigns each set of coordinates  $(a, b, c) \in \mathbb{N}^3$  a position  $\mathcal{I}(a, b, c) \in \mathbb{N}$  in the data vector.

The derivative of the field can now be approximated by a weighted difference of the values of  $\vec{F}$ . To illustrate this, w.l.o.g., the derivative in the  $x$  direction in (11) is considered

$$\partial_x \vec{f}_{a,b,c} = \sum_{\nu} \mathcal{S}_{\nu} \vec{f}_{a+\nu,b,c} + \mathcal{O}(\Delta_x^n), \quad (12)$$

where the order of accuracy  $n$  is given by the choice of the stencil  $\widehat{\mathcal{S}}$  with elements  $\mathcal{S}_n$ . The size of the stencil is defined as

$$|\widehat{\mathcal{S}}| = |\{n \in \mathbb{Z} \mid \mathcal{S}_n \neq 0\}|. \quad (13)$$

Upwind differencing of the 1st derivative of an arbitrary function  $g$  to 2nd order implies [21]

$$\frac{\partial g(x)}{\partial x} = \frac{g(x + \Delta_x) - g(x)}{\Delta_x}. \quad (14)$$

The corresponding stencil is defined as

$$\mathcal{S}_0 = \mathbf{1} \left( -\frac{1}{\Delta_x} \right), \quad \mathcal{S}_1 = \mathbf{1} \frac{1}{\Delta_x}, \quad \mathcal{S}_i = 0 \quad \forall i \notin \{0, 1\} \quad (15)$$

and has the size  $|\widehat{\mathcal{S}}| = 2$ . In the case of the downwind differencing

$$\frac{\partial g(x)}{\partial x} = \frac{g(x) - g(x - \Delta_x)}{\Delta_x} \quad (16)$$

the corresponding stencil is defined as

$$\mathcal{S}_{-1} = \mathbf{1} \left( -\frac{1}{\Delta_x} \right), \quad \mathcal{S}_0 = \mathbf{1} \frac{1}{\Delta_x}, \quad \mathcal{S}_i = 0 \quad \forall i \notin \{-1, 0\}. \quad (17)$$

There are two things to be considered when choosing  $\widehat{\mathcal{S}}$ . Firstly, with larger size of the stencil both, the accuracy of the numerical scheme and the numerical load of the algorithm increase. For the solver presented in this paper 4th order differences are used. The second consideration to be made is biasing. Choosing a symmetric distribution  $\mathcal{S}_{-k} = \mathcal{S}_k$  of stencil points leads to  $\mathcal{S}_0 = 0$  causing two disconnected grids. Disconnected grids cause mesh drift instabilities [21]. Avoiding the latter by biasing the stencil, i.e., by taking an asymmetric stencil

results in an anisotropic space, which reduces the propagation speed of em-waves in the direction towards which the stencil is heavier weighted.

While the mesh drifting cannot be avoided for symmetric stencils propagation speed errors due to biased stencils however can. To see this the expression

$$\begin{pmatrix} 0 & \mathbf{Q}_x \\ -\mathbf{Q}_x & 0 \end{pmatrix} = \mathbf{R}_x^T \text{diag}(0, 1, 1, 0, -1, -1) \mathbf{R}_x \quad (18)$$

in (11) is first diagonalized, where

$$\mathbf{R}_x = \frac{1}{\sqrt{2}} \begin{pmatrix} 0 & 0 & 0 & 0 & 0 & 0 \\ 0 & 1 & 0 & 0 & 0 & -1 \\ 0 & 0 & 1 & 0 & 1 & 0 \\ 0 & 0 & 0 & 0 & 0 & 0 \\ 0 & 1 & 0 & 0 & 0 & 1 \\ 0 & 0 & 1 & 0 & -1 & 0 \end{pmatrix} \quad (19)$$

leading with the help of (12) to

$$\begin{pmatrix} 0 & \mathbf{Q}_x \\ -\mathbf{Q}_x & 0 \end{pmatrix} \partial_x \vec{f} \approx \begin{pmatrix} 0 & \mathbf{Q}_x \\ -\mathbf{Q}_x & 0 \end{pmatrix} \mathcal{D}_x \vec{f}_{a,b,c}, \quad (20)$$

where

$$\mathcal{D}_x \vec{f}_{a,b,c} = \sum_{\nu} \mathbf{R}_x^T \mathcal{S}_{\nu} \mathbf{R}_x \vec{f}_{a+\nu,b,c}, \quad \mathbf{R}_x \vec{f} = \frac{1}{\sqrt{2}} \begin{pmatrix} 0 \\ E_y - B_z \\ E_x + B_y \\ 0 \\ E_y + B_z \\ E_z - B_y \end{pmatrix}. \quad (21)$$

Equations (18) and (21) imply that in the rotated frame the solution of (11) propagates only in the direction, which is given by the sign of the eigenvalues of the diagonal matrix in equation (18). This implies that  $E_y - B_z$  and  $E_x + B_y$  both propagate along the positive  $x$ -direction while  $E_y + B_z$  and  $E_z - B_y$  propagate along the negative  $x$ -direction. Choosing downwind biasing for fields propagating along the positive  $x$ -axis, upwind biasing for fields propagating along the negative  $x$ -axis and rotating back afterwards suppresses the propagation speed error. As a consequence no mesh drifting and no propagation speed asymmetry are expected.

Making use of the up- and downwind stencils to 2nd order as defined in (15) and (17) for  $\mathbf{R}_x \vec{f}$  for the different directions of em-wave propagation results in the following matrices for the stencil elements

$$\begin{aligned}\mathcal{S}_{-1} &= \text{diag}(0, -1, -1, 0, 0, 0) \frac{1}{\Delta_x}, \\ \mathcal{S}_0 &= \text{diag}(0, 1, 1, 0, -1, -1) \frac{1}{\Delta_x}, \\ \mathcal{S}_1 &= \text{diag}(0, 0, 0, 0, 1, 1) \frac{1}{\Delta_x}, \\ \mathcal{S}_i &= 0 \quad \forall i \notin \{-1, 0, 1\}.\end{aligned}\tag{22}$$

A compact notation for (22) is

$$\begin{aligned}\mathcal{S}_\nu &= \text{diag}(0, s_\nu^+, s_\nu^+, 0, s_\nu^-, s_\nu^-) \frac{1}{\Delta_x}, \\ s_\nu^+|_{\nu=-1, \dots, 1} &= \{-1, 1, 0\} \\ s_\nu^-|_{\nu=-1, \dots, 1} &= \{0, -1, 1\} \\ s_\nu^{+/-} &= 0 \quad \forall \nu : |\nu| > 1.\end{aligned}\tag{23}$$

The stencils used in the simulations in the present paper are accurate up to the 4th order, where the values of the stencils at the diagonals  $s_\nu^+$  and  $s_\nu^-$  in the forward + and backward - directions are given by

$$\begin{aligned}s_\nu^+|_{\nu=-3, \dots, 3} &= \left\{ -\frac{1}{12}, \frac{1}{2}, -\frac{3}{2}, \frac{5}{6}, \frac{1}{4}, 0, 0 \right\}, \\ s_\nu^-|_{\nu=-3, \dots, 3} &= \left\{ 0, 0, -\frac{1}{4}, -\frac{5}{6}, \frac{3}{2}, -\frac{1}{2}, \frac{1}{12} \right\}, \\ s_\nu^{+/-} &= 0 \quad \forall \nu : |\nu| > 3.\end{aligned}\tag{24}$$

Note that the rotation matrices will always sort the eigenvalues of  $\text{adiag}(-\mathbf{Q}_i, \mathbf{Q}_i)$ , where  $i = x, y, z$  in the same way and thus the  $\mathcal{S}_\nu$  is identical in all three spatial directions.

#### 4.2. Nonlinear case

Using the same approach for equations (8a) and (8b) yields

$$\partial_t \vec{f} = (\mathbf{1} + \mathbf{A})^{-1} \sum_i \mathbf{B}_i \partial_i \vec{f},\tag{25}$$

where

$$\mathbf{A} = \begin{pmatrix} \mathbf{J}_{\vec{F}}(\vec{E}) & \mathbf{J}_{\vec{F}}(\vec{B}) \\ 0 & 0 \end{pmatrix},\tag{26}$$

$$\mathbf{B}_i = \begin{pmatrix} -\mathbf{Q}_i \mathbf{J}_{\vec{M}}(\vec{E}) & \mathbf{Q}_i (\mathbf{1} - \mathbf{J}_{\vec{M}}(\vec{B})) \\ -\mathbf{Q}_i & 0 \end{pmatrix}\tag{27}$$

and  $\mathbf{J}_{\vec{A}}(\vec{B})$  is the Jacobi matrix of  $\vec{A}$  with respect to  $\vec{B}$ . The problem now is that the eigenvectors of the  $\mathbf{B}_i$  are no longer constant since they depend on the em-fields. This implies that the matrices  $\mathbf{R}_i$  with  $i = x, y, z$  depend on the em-field configuration and cannot be easily calculated analytically. However, the nonlinear corrections due to  $\mathbf{A}$  and  $\mathbf{B}$  in (25) are small. As a consequence the effect of the nonlinear contributions in (25) on the eigenvalues and eigenvectors of the matrix  $\mathbf{B}$  can be neglected. Thus, the same rotations used for the derivatives in the linear case can be used and the numerical artifacts due to biasing are still suppressed in the nonlinear case. By the same rationale the matrix inversion in (25) can be performed by using the geometrical series  $(\mathbf{1} + \mathbf{A})^{-1} = \mathbf{1} - \mathbf{A} + \mathbf{A}^2 - \mathcal{O}(\mathbf{A}^3)$  and neglecting higher order terms. This approximation is justified since contributions from the higher order terms fall below the desired accuracy.

The nonlinear scheme is

$$\partial_t \vec{f} = (\mathbf{1} - \mathbf{A}) \sum_i \mathbf{B}_i \mathcal{D}_i \vec{f}, \quad (28)$$

$$\mathcal{D}_x \vec{f} = \sum_\nu \mathbf{R}_x^T \mathcal{S}_\nu \mathbf{R}_x \vec{f}_{a+\nu, b, c}, \quad (29)$$

$$\mathcal{D}_y \vec{f} = \sum_\nu \mathbf{R}_y^T \mathcal{S}_\nu \mathbf{R}_y \vec{f}_{a, b+\nu, c}, \quad (30)$$

$$\mathcal{D}_z \vec{f} = \sum_\nu \mathbf{R}_z^T \mathcal{S}_\nu \mathbf{R}_z \vec{f}_{a, b, c+\nu}, \quad (31)$$

where

$$\mathbf{R}_x = \frac{1}{\sqrt{2}} \begin{pmatrix} \sqrt{2} & 0 & 0 & 0 & 0 & 0 \\ 0 & 1 & 0 & 0 & 0 & -1 \\ 0 & 0 & 1 & 0 & 1 & 0 \\ 0 & 0 & 0 & \sqrt{2} & 0 & 0 \\ 0 & 1 & 0 & 0 & 0 & 1 \\ 0 & 0 & 1 & 0 & -1 & 0 \end{pmatrix}, \quad \mathbf{R}_x \vec{f} = \frac{1}{\sqrt{2}} \begin{pmatrix} \sqrt{2} E_x \\ E_y - B_z \\ E_x + B_y \\ \sqrt{2} B_x \\ E_y + B_z \\ E_z - B_y \end{pmatrix} \quad (32)$$

and

$$\mathbf{R}_y = \frac{1}{\sqrt{2}} \begin{pmatrix} 0 & \sqrt{2} & 0 & 0 & 0 & 0 \\ -1 & 0 & 0 & 0 & 0 & -1 \\ 0 & 0 & -1 & 1 & 0 & 0 \\ 0 & 0 & 0 & 0 & \sqrt{2} & 0 \\ -1 & 0 & 0 & 0 & 0 & 1 \\ 0 & 0 & -1 & -1 & 0 & 0 \end{pmatrix}, \quad \mathbf{R}_y \vec{f} = \frac{1}{\sqrt{2}} \begin{pmatrix} \sqrt{2} E_y \\ -B_z - E_x \\ B_x - E_z \\ \sqrt{2} B_y \\ B_z - E_x \\ -B_x - E_z \end{pmatrix} \quad (33)$$



and

$$\mathbf{R}_z = \frac{1}{\sqrt{2}} \begin{pmatrix} 0 & 0 & \sqrt{2} & 0 & 0 & 0 \\ 1 & 0 & 0 & 0 & -1 & 0 \\ 0 & 1 & 0 & 1 & 0 & 0 \\ 0 & 0 & 0 & 0 & 0 & \sqrt{2} \\ 1 & 0 & 0 & 0 & 1 & 0 \\ 0 & 1 & 0 & -1 & 0 & 0 \end{pmatrix}, \quad \mathbf{R}_z \vec{f} = \frac{1}{\sqrt{2}} \begin{pmatrix} \sqrt{2} E_z \\ -B_y + E_x \\ B_x + E_y \\ \sqrt{2} B_z \\ B_y + E_x \\ -B_x + E_y \end{pmatrix}. \quad (34)$$

Due to the nonlinear contributions coupling to the derivative in propagation direction the stencils become

$$\mathcal{S}_\nu = \text{diag} (s_\nu^+, s_\nu^+, s_\nu^+, s_\nu^-, s_\nu^-, s_\nu^-) \frac{1}{\Delta}, \quad (35)$$

where  $\Delta$  are the spatial resolutions along the directions  $x, y, z$ .

#### 4.3. Solving the ODE and processing the data

The ODE for the propagation of light defined by (25) can now be solved by any generic ODE solver. In this paper the *CVODE* solver from the *SUNDIALS* bundle is used [22]. The post-processing of the simulation data for this paper has been performed with *Mathematica* [23].

#### 4.4. Parallelisation of the algorithm

The numerical method presented in this paper can be parallelized. In order to distribute the computational load over multiple processing cores the lattice is sliced into smaller sub-lattices. The communication between compute nodes is limited to the exchange of boundary values for the computation of the discrete space derivatives in (28). The computation of the right hand side of (28) and the subsequent time step update are then a purely local problem.

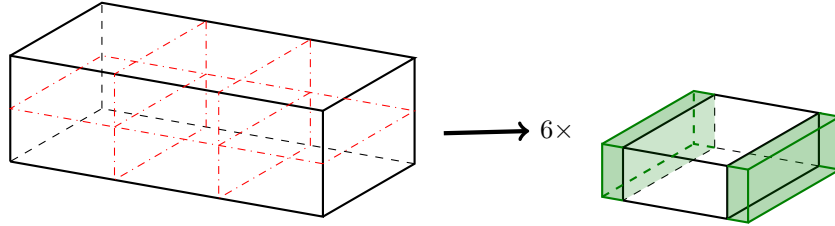


Figure 2: Sketch of a lattice decomposition (left) into 6 lattice patches. The red dashdotted lines indicate the boundaries of the lattice patches. The green cuboids attached to the lattice patch (right) are the ghost layers that store the values from neighboring patches. For better visibility only the ghost layers in one direction are shown.

## 5. Properties of the numerical scheme

### 5.1. Propagation error and dispersion relation for the linear case

The pulse propagation in the QED vacuum reduces to the usual propagation in vacuum when only a single plane wave is present. Furthermore, the propagation error scales as  $\mathcal{O}(\Delta^4)$ . As the derivative in time is solved using a recursive implicit algorithm it can be assumed that the time derivative is exact. When inserting the plane wave

$$\vec{E}(\vec{x}, t) = \vec{\varepsilon} e^{-i(\omega t - \vec{k} \cdot \vec{r})}$$

in (25), where  $\vec{\varepsilon}$  is the polarization vector of the latter, and solving for the dispersion relation it is obtained

$$0 = \det \left( i\omega \mathbf{1}_6 - \sum_{j \in \{x, y, z\}} \text{adiag}(\mathbf{Q}_j, -\mathbf{Q}_j) \mathbf{R}_j^\top \sum_{\nu} S_{\nu} e^{-i\nu k_j \Delta_j} \mathbf{R}_j \right). \quad (36)$$

The  $S_{\nu}$  are the values of the stencils as introduced in section 4. Note that the rotation matrices  $\mathbf{R}_j$  in (36) disappear. Equation (36) is evaluated numerically.

The results are shown in Figure 3. Figure 3(left) shows the frequency depen-

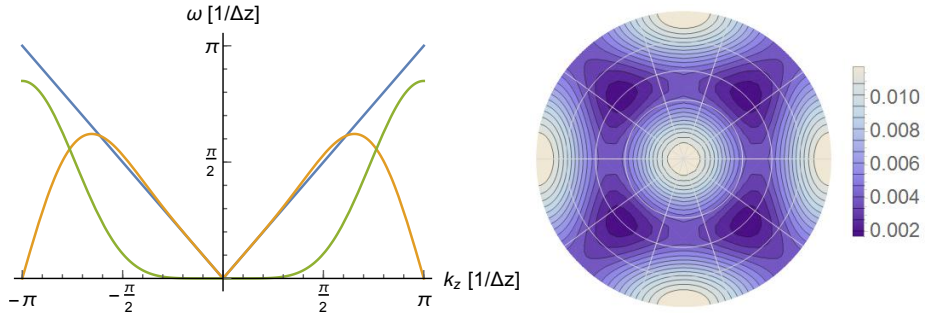


Figure 3: Left:  $\omega$  vs.  $k_z$  for a plane wave with  $\vec{k} = (00 k_z)^T$ . The blue line is the dispersion relation of the continuous vacuum. The orange one is the real part of  $\omega$  as computed in (36) and the green one is the imaginary part. Right: Spherical polar plot of the real part of  $\omega$  minus the  $\omega$  in the continuous vacuum in 3D. The radial coordinate is  $\theta$  with  $0 \leq \theta < \pi$  and the angular variable is  $\phi$  with  $0 \leq \phi < 2\pi$ . Note that  $|\vec{k}|$  has been set to  $0.8/z$ . Larger values (brighter colors) imply that the wave propagates faster in that direction.

dence of the dispersion relation in  $z$ -direction. It can be seen that the dispersion is well behaved for small  $\Delta |\vec{k}| \ll 1$ . Furthermore, as  $|\vec{k}|$  grows, i.e., the wavelength becomes smaller, the phase velocity of the em-wave is above the light speed. On top of that, the imaginary part of  $\omega$ , which causes the lattice to absorb the electromagnetic field is negligible for small  $|\vec{k}|$  but becomes relevant at higher frequencies.

The dependence of the phase velocity on the propagation direction of the wave is illustrated in figure 3(right). As can be seen in the figure the wave

propagates fastest along the discretization directions  $[1, 0, 0]$ ,  $[0, 1, 0]$  and  $[0, 0, 1]$ . This is an expected behaviour for all Cartesian grid discretizations [21, 24]. The phase velocity is lowest along the diagonal  $[1, 1, 1]$ . The difference between  $[1, 1, 1]$  and  $[1, 0, 0]$  scales as  $\mathcal{O}(|\vec{k}|^3)$  and reaches a relative maximum of 1% for frequencies below half of the Nyquist frequency given by  $f_{\text{Ny}} = \pi/2\Delta_z$ .

### 5.2. The computational load

There are three key steps in the application of the algorithm: (i) The computation of the derivatives, (ii) the computation on the right hand side of (25), and (iii) the integration of the ODE.

While the number of operations involved in (i) for computing the approximation of the space derivatives does not depend on the number of lattice points considered, the derivatives have to be calculated for each point separately and for each of the dimension considered

$$\mathcal{W}_D \propto D \cdot N_x \cdot N_y \cdot N_z, \quad (37)$$

where  $\mathcal{W}_D$  is the computational load. A similar scaling holds for an integration step of (25) addressed in (ii). The number of spatial dimensions  $D$  determines the number of summations. The right hand side of (28) has to be evaluated for each grid point of the lattice and thus the scaling becomes

$$\mathcal{W}_M \propto N_x \cdot N_y \cdot N_z \cdot (D + 1), \quad (38)$$

where  $\mathcal{W}_M$  is the computational load encountered for the evaluation of (25). We note that the term plus one in (38) comes from the multiplication of the sum with the  $(1 - A)$  matrix in (25).

The load for the solution of the ODE (iii) depends on the choice of the solver. For the *CVODE* solver used in the present paper details can be found in [22]. However, as the integration of the ODE in (25) strongly depends on the problem under consideration its scaling depends on the frequencies involved, the strength of the nonlinearities, the precision required and so on

$$\mathcal{W}_S \propto \frac{1}{\Delta} N_x \cdot N_y \cdot N_z, \quad (39)$$

where  $\mathcal{W}_S$  is the computational load of the *CVODE* solver. Summarizing, an upper limit for the scaling of the problem is given by

$$\mathcal{W} \propto \frac{1}{\Delta} N_x \cdot N_y \cdot N_z \cdot (D + 1). \quad (40)$$

### 5.3. Comparison to the Yee algorithm

Comparison of the properties of the numerical scheme in the present paper to the classical Yee solver for Maxwell's equations [24] shows several major differences apart from the obvious increase in computational load since the scheme in this paper is implicit and of 4th order accuracy while the Yee solver is explicit and of 2nd order accuracy only. The major differences are

- i The computation of the nonlinearities in (28) does not require the extra effort of interpolating field values as the scheme in this paper does not make use of a staggered grid.
- ii Since the numerical dispersion relation of the scheme in the present paper has an imaginary part aliasing modes are suppressed. This is not the case for the Yee scheme.
- iii The use of 4th order stencils in the scheme in this paper allows for 4th order accuracy of the present scheme while Yee is only 2nd order.
- iv Through the use of propagation direction dependent biasing of the stencils in space a symmetric dispersion relation is achieved while mesh drifting is avoided. Staggering the grid as is done in the Yee scheme also avoids mesh drifting but causes loss of information needed for the computation of nonlinearities.

## 6. Benchmarking with analytical solutions

The easiest test that can be performed to validate the accuracy and efficiency of the numerical algorithm in the present paper is to check it against the linear case. As  $\mathcal{L}_{HE}$  vanishes for a single planar laser pulse, the latter will propagate in the QED vacuum as it would in the classical vacuum. The analytical solution for this case is

$$\vec{E}(\vec{x}, t) = \vec{E} \left( \vec{x} - \frac{1}{3} \left( \frac{\omega}{k_x}, \frac{\omega}{k_y}, \frac{\omega}{k_z} \right) t, 0 \right), \quad (41)$$

where  $\vec{k}$  is the wavenumber and  $\omega/|\vec{k}|$  the phase velocity. Equation (41) can be compared to simulation results to determine the linear dispersion errors generated by the discretisation.

To validate the algorithm for the nonlinear part of the vacuum wave equations numerical results are compared to those derived analytically for some of the nontrivial effects of the nonlinear QED vacuum, a comprehensive collection of which can be found in [25].

In the present paper the flip of polarization and the generation of higher harmonics are considered because they are two of the most well know and best studied effects in literature. In addition, the main contribution to polarization flips are due to 4-photon while the asymptotic 2nd harmonics are due to 6-photon diagrams as depicted in figure 1. Hence, both 4- and 6-photon contributions can be tested numerically.

### 6.1. High harmonic generation

High harmonic generation is a direct consequence of energy conservation. To see this the 4-photon scattering diagram in figure 1 is considered. If the two legs to the left of the diagram represent two incoming probe photons with  $\omega_p$  and the third leg represents the contribution of the pump photon  $\omega_b$  the frequency of the resulting photon has to be  $\omega_R = \omega_b + 2\omega_p$  as is shown in figure

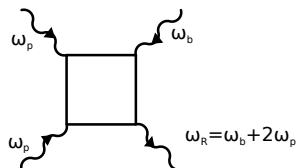


Figure 4: Generation of higher harmonics due to 4-photon interaction. The two incoming photons to the left come from the probe  $p$  and the incoming photon on the right comes from the strong background  $b$ . The frequency of the exiting photon has to be  $\omega_R = \omega_b + 2\omega_p$  due to energy conservation.

4. As analytical estimates in 1D show 2nd harmonics generation is expected to be several orders of magnitude smaller than polarization flipping. However, it is expected to be more sensitive to the pulse shapes involved in the interaction. In order to benchmark the numerical results of 2nd harmonic generation the calculations presented in [9] are used for reference.

### 6.2. Polarization flipping

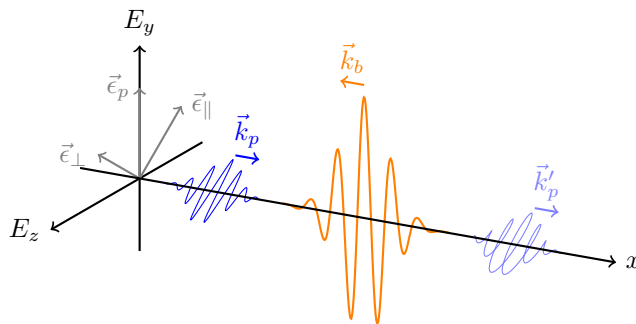


Figure 5: Qualitative sketch of the electric fields in a coaxial background-probe experiment for measuring vacuum birefringence. The probe (blue) travels through the counter-propagating background (orange) experiencing a polarisation flip due to the different refractive indices for different polarization directions (42).

Polarization flipping is a result of vacuum birefringence. Here the polarization of the strong background breaks the isotropy of space. This gives rise to the different refractive indices for parallel and perpendicular polarizations of the probe in relation to the background [26, 15]

$$n_{\parallel} = 1 + \frac{8\alpha}{45\pi} \frac{E^2}{E_{cr}^2}, \quad n_{\perp} = 1 + \frac{14\alpha}{45\pi} \frac{E^2}{E_{cr}^2}. \quad (42)$$

The refractive indices in (42) generate a difference in the optical path length for parallel and perpendicular polarizations, which is the cause of the flipping. The refractive indices (42) have been derived making use of 4-photon interaction only, i.e., all but the first term in (4) have been neglected.

The typical proposal for a setup for measuring flipping consists of two coaxially [14] or nearly coaxially [27, 28] propagating pulses, one of the two is a strong infrared (IR) background pulse and the other a weak counter-propagating hard x-ray probe. A depiction of this setup is shown in figure 5.

There are numerous analytical results of polarization flipping in the literature. In the present paper the work published in [14, 15] is used for benchmarking the efficiency and accuracy of the algorithm. In particular, the flipping probabilities for the settings in [14] and the parametric dependencies derived in [15] are reproduced.

## 7. Numerical results

### 7.1. High harmonic generation

As can be seen in figure 6 there is good agreement between the analytic approximation and our simulation results of 2nd harmonic generation. The relative error between numerical and analytical results is less than 3%. While this error is worse than in our numerical calculations of polarization flipping (see below) it has to be noted, that the effect of high harmonic generation is of much smaller relative magnitude and thus suffers more from errors in numerical calculations. Furthermore, a simulation with  $\omega_b \neq 0$  allows to visualize the

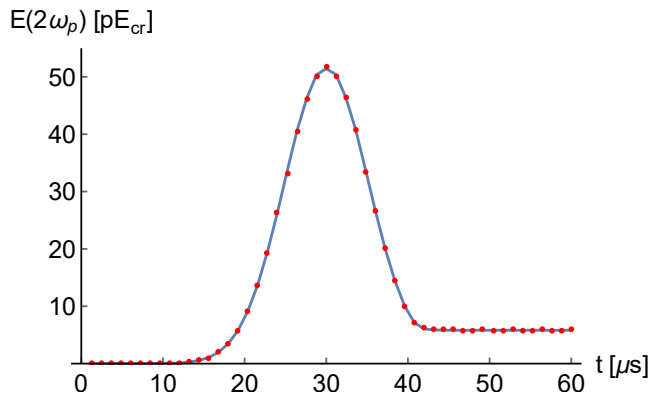


Figure 6: Plot of the amplitude of the 2nd harmonic of the electric field versus time. The dots represent the simulation data while the solid line is the analytic approximation derived in [9]. The error for all simulated data points lies below 3%. At  $t = 60\mu s$  the probe has traversed the background implying that the signal represents the asymptotic 2nd harmonic.

200  $2\omega_p \pm \omega_b$  signal in the overlap field, which comes from the 4-photon interaction and the  $2\omega_p$  signal in the asymptotic field at  $t > 50\mu s$ . The latter is generated by the 6-photon contribution. This shows that the algorithm allows to time resolve the different processes.

Sim. Box	Size	80 $\mu\text{m}$
Pump Pulse	$ \vec{E} _{\text{max}}$	0.34 $mE_{cr}$
	$\hat{k}$	(-1, 0, 0)
	$x_0$	60 $\mu\text{mm}$
	$\lambda$	800 nm
	$f$	1.54 eV
	$t$	30 fs
Probe Pulse	$ \vec{E} _{\text{max}}$	0.05 $mE_{cr}$
	$\hat{k}$	(1, 0, 0)
	$x_0$	20 $\mu\text{mm}$
	$\lambda$	96 pm
	$f$	12.9 keV
	$t$	30 fs

Table 1: Parameters for probe and background beams presented in [14]. We note that the background and probe pulses are coaxially counter-propagating. Furthermore, the background and probe pulse polarization are at an angle of  $\pi/4$  to each other and the peak to peak distance between the pulses at  $t = 0$  is 40  $\mu\text{m}$ .

## 7.2. Polarisation flipping: Experimental expectations

For case (a) defined in [14] the pulse parameters are given in table 1. It is worth noting that there are a couple of considerations to make when simulating the setup presented in [14]. Firstly, since a 1D simulation is used for case (a) in [14] in the present paper there is no lateral dispersion of the background field. In order to account for the lateral dispersion assumed in [14] the field strength in our simulation needs to be reduced to the average field intensity over the interaction time  $t_i$  (see figure 7). Secondly, since in [14] the probe pulse is an x-ray pulse a large number of grid points,  $N_{\text{Point}} \approx 10^7$ , is required to remain below the Nyquist frequency, i.e., to avoid numerical artifacts due to the undersampling of the oscillations. In order to avoid running such large and expensive simulations a number of simulations with larger wavelengths for the probe pulse (50 nm, 100 nm, 200 nm, 400 nm, 600 nm) are run and the flipping values are then extrapolated from these results to x-ray wavelength.

Finally, as em-fields are being simulated instead of single photons the only accessible data are the field values at any given time. To compare these results to the ones in paper [14] the energies in each polarization direction are computed as

$$\mathcal{E}_{\perp} = \sum_{x_i \in \mathcal{B}} \left( \vec{E}(x_i) \cdot \vec{\epsilon}_{\perp} \right)^2, \quad \mathcal{E}_{\parallel} = \sum_{x_i \in \mathcal{B}} \left( \vec{E}(x_i) \cdot \vec{\epsilon}_{\parallel} \right)^2, \quad \mathcal{E}_{\text{tot}} = \mathcal{E}_{\perp} + \mathcal{E}_{\parallel}. \quad (43)$$

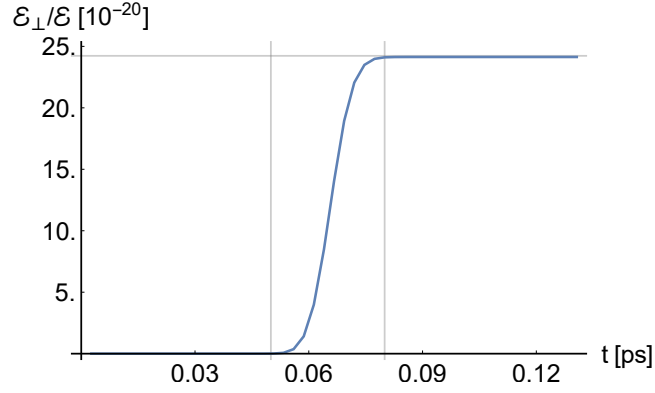


Figure 7: Time evolution of the polarisation flipping for the parameters presented in Tab.1 with increased wavelength for the probe pulse ( $\lambda_p = 400$  nm). The distance between the vertical lines corresponds to the interaction time  $t_i$ , within which 96% of the polarisation flip occurs. The horizontal line notes the asymptotic relative flipping energy.

It can easily be checked, that

$$\frac{N_\perp}{N} = \frac{\hbar\omega N_\perp}{\hbar\omega N} = \frac{\mathcal{E}_\perp}{\mathcal{E}_{tot}}, \quad (44)$$

where  $N$  and  $N_\perp$  are the number of total and perpendicular photons contained in the probe beam.

Running the simulations using the algorithm presented in section 4 and extrapolating the results assuming a  $1/\lambda^2$  scaling yields  $N_\perp/N = 1.42 \cdot 10^{-12}$  (see figure 8), which represents a deviation of less than 2% from the value obtained by Karbstein et. al. ( $N_\perp/N = 1.39 \cdot 10^{-12}$ ) in [14].

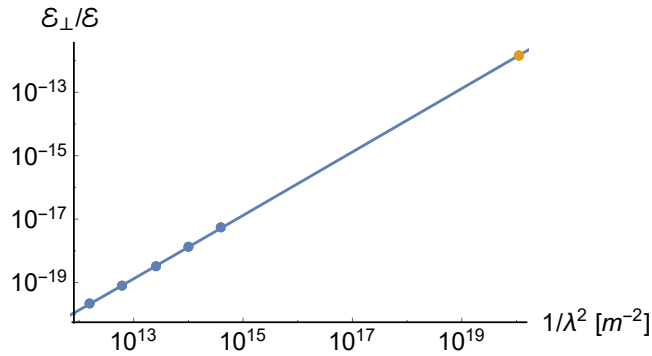


Figure 8: Extrapolation of the wavelength in dependence of the polarisation flipping energy. The blue dots represent the relative polarisation energy at 800 nm, 400 nm, 200 nm, 100 nm and 50 nm from left to right. The solid blue line is the linear interpolation of these points with  $1/\lambda_p^2$  as the linear variable. The orange point is the value given in [14].



### 7.3. Polarisation flipping: Parametrical dependencies

For coaxially counter-propagating background and probe pulses the polarisation flipping probability is given in the low energy approximation  $p_b p_p \ll m^2$ , where  $p_b$  is the momentum of the background and  $p_p$  the one of the probe pulse, by [15]

$$\mathbf{P}_{\text{flip}} = \frac{\alpha^2}{225} \frac{1}{\lambda_p^2} \sin^2(2\sigma) \left( \int dx^+ \vec{E}(x^+)^2 \right)^2, \quad (45)$$

where  $\sigma$  is the angle between the probe and background polarizations. The main consequence of (45) is the fact that the pulse flipping probability depends solely on the background pulse energy for any pulse shape. Besides that it states that the flipping probability only depends on  $\sigma$  and  $\lambda_p$ .

In order to verify that the probability for flipping depends only on the pulse energy a set of different background and probe profiles with the same energy,  $\sigma$ , and  $\lambda_p$  (see figure 9) is chosen.

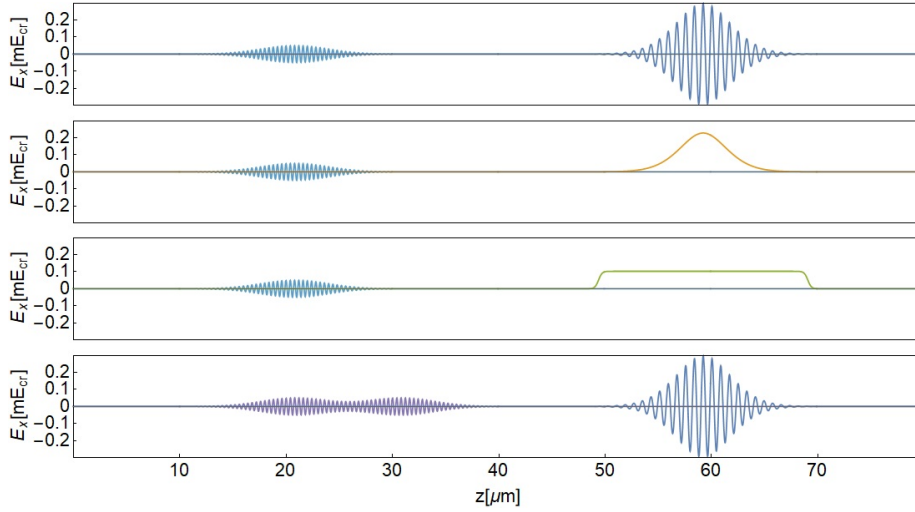


Figure 9: Different initial settings for the electric fields simulated. The parameters  $\sigma$ ,  $\lambda_p$ , and  $\mathcal{E}_b$  are the same for all the settings. The reference setting (blue, top) is the one used for the reproduction of the results given in [14] with  $\lambda_p = 400$  nm, see 7.2. Then, there are the 0-frequency background (orange, 2nd from top), the shock regime background (green, 3rd from top), and the chirped probe (purple, bottom). The color scheme corresponds to the one used in figure 10.

As figure 10 shows the statement holds for the asymptotic field, but the form of the polarization flip during the interaction and the duration of the interaction vary heavily.

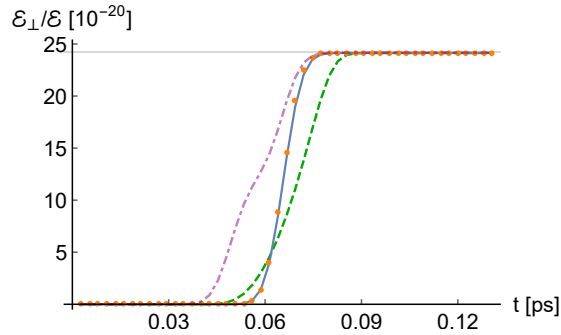


Figure 10: Plot of the relative flipping amplitude versus time for the different backgrounds shown in figure 9. The color scheme is the same as in figure 9. The relative numerical error for the asymptotic value (horizontal line) computed with the help of relation (45) is less or equal than 0.5% for all the cases.

The reproduction of the  $\lambda_p$  scaling by the algorithm can be seen in figure 8. The  $\sigma$  and energy scalings remain to be checked. Different values for the peak field strength  $A$  and relative polarization angle  $\sigma$  starting with the parameters given in table 1 and  $\lambda_p = 400$  nm are simulated. The results are shown in figure 11.

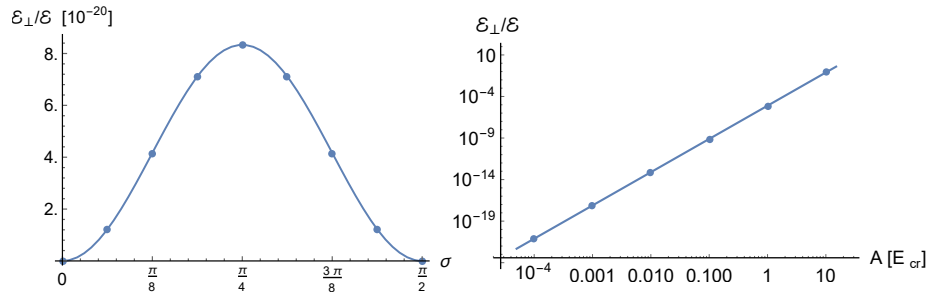


Figure 11: Left: Plot of the relative polarization flipping vs. angle  $\sigma$  between probe and background pulse polarizations using the settings from table 1 with  $\lambda_p$  set to 400 nm. The dots are the values obtained via simulation and the solid line is the prediction using (45). Note that the relative error is less or equal to 0.3% for all data points. Right: Plot of relative polarization flipping vs. background pulse amplitude  $A$  using the parameters from table 1 with  $\lambda_p$  set to 400 nm. The dots are the values gained with the help of simulations and the solid line is the prediction using (45). The relative error is less or equal to 0.3% for all data points.

Besides the small error between numerical and analytical results of 0.3% in all simulations the flipping probability is  $1.2 \cdot 10^{-27}$  at  $\sigma = \pi/2$ , which is larger than the numerical noise of  $\sim 4 \cdot 10^{-33}$ . The signal of the flipping probability at  $\pi/2$  should not be there according to (45). It is due to high harmonic generation neglected in the analytical derivation of the flipping probability in (45). Furthermore, extreme testing of the numerical algorithm shows, that it

remains stable up to  $A = 100 E_{cr}$ , which is well beyond the limits of the weak field expansion.

#### 7.4. Parallelization scaling

Measurements of weak scaling show a  $1.09 \cdot \#_{cores}$  dependence on the total core time. Similarly, a factor of 1.04 is measured for strong scaling.

## 8. Results in higher dimensions

Having verified the validity of the algorithm the next step is to simulate higher dimensions. The first simulation in higher dimensions is the collision of two coaxial Gaussian pulses in 2D (see figure 12). As in the 1D case the generation of higher harmonics is observed due to the inclusion of the 6-photon scattering diagram in the numerical simulation. Furthermore, the sharpening of the pulses as predicted by [14] is observed in the asymptotic field.

A feature-rich simulation is shown in figure 13. The pulses in the figure are no longer propagating along the same axis. As a result a myriad of mixing processes caused by the 4-photon interaction opens up. Once again, it can be observed how these signatures vanish in the asymptotic fields. It is, however, worth noting that contrary to the 1D case the asymptotic  $3\omega_p$  signal is slightly off axis causing it to split off from the main pulse.

Furthermore, it is verified via turning off the 4- and 6-photon scattering diagrams separately, that the higher harmonic signal in the asymptotic field is once again solely generated by the 6-photon scattering while the 4-photon contribution does not generate anything beyond scattering signals in the  $\omega = \omega_p$  spectral region. Note that in the orthogonal case the signal is not symmetric along the  $\omega_x = 0$  and  $\omega_y = 0$  axes. However, symmetry is conserved along the symmetry axes  $\omega_x + \omega_y = 0$ , which corresponds to the initial symmetry of the setup.

It has to be mentioned that the symmetry of the simulated fields has to be conserved by a accurate and consistent numerical algorithm. This statement is of the utmost importance as it would be clearly non-physical to violate basic symmetries of the underlying equations. Symmetry violation is a clear sign that an algorithm is not working properly.

## 9. Discussion and conclusion

A numerical solver for the nonlinear Heisenberg-Euler wave equations has been derived. Only two approximations have been made: (i) The wavelengths involved are larger than the Compton wavelength and (ii) the involved fields are weaker than the critical field strength  $E_{cr}$ . Furthermore, we have shown that the numerical results agree with a range of analytic results derived in the literature [9, 10, 14, 15].

It is astonishing that there is excellent agreement between the simulation results and the analytic benchmarks, since in [14] and in [15] the x-ray probes are

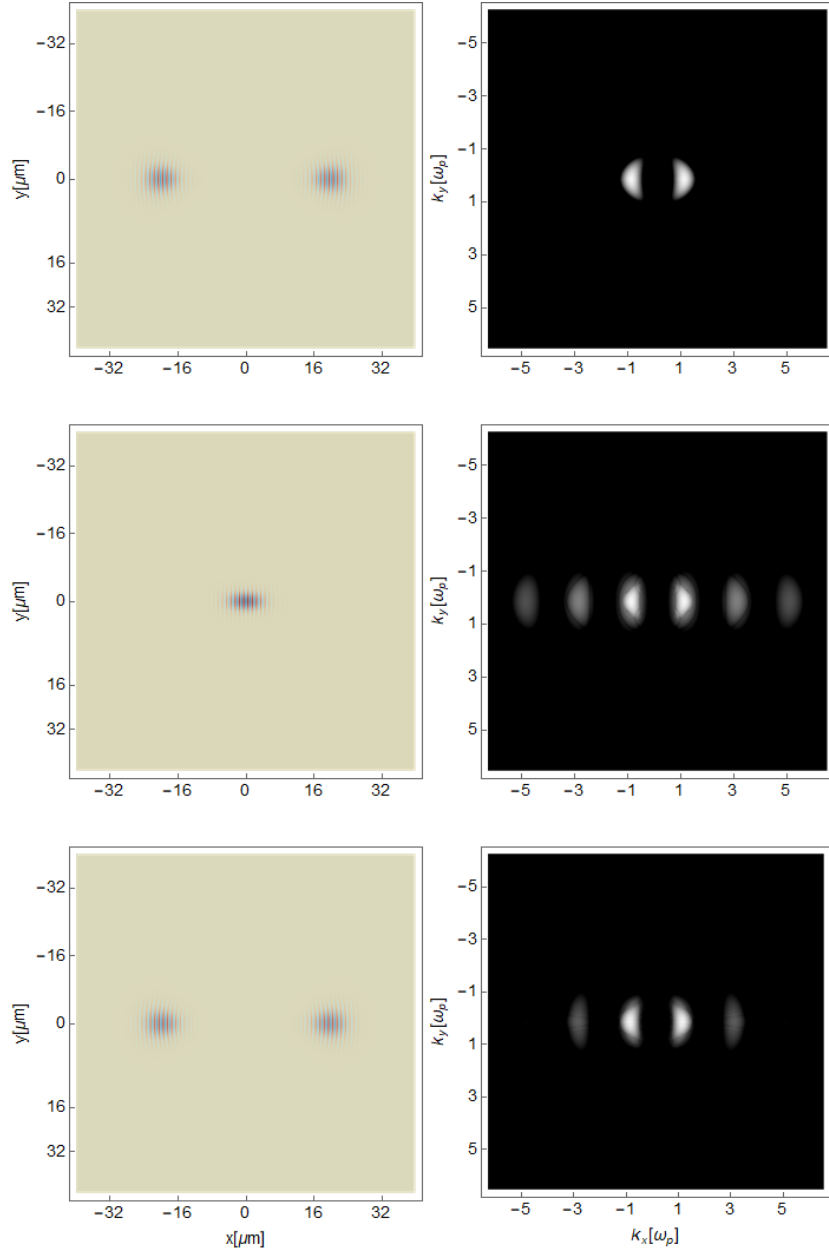


Figure 12: Plots of simulated values for  $E_z$  for two coaxially propagating Gaussian pulses with  $E_0 = 0.05E_{cr}$ . The plots to the left are in physical space and the ones to the right are in frequency space. The two in the top are the initial settings, the ones in the middle show the overlap state, and the ones in the bottom represent the field configuration after the collision.

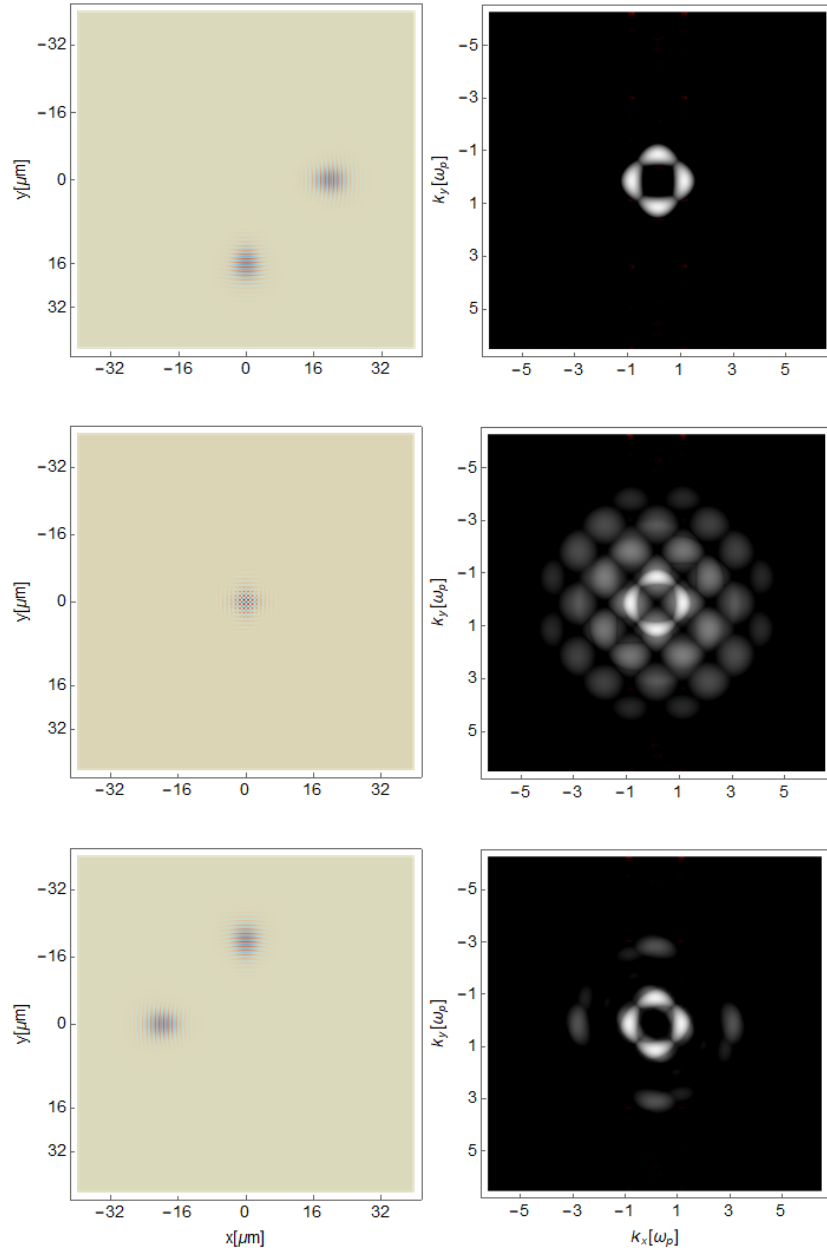


Figure 13: Plots of simulated values for  $E_z$  for two orthogonally propagating Gaussian pulses with  $E_0 = 0.05E_{cr}$ . The plots to the left are in physical space and the ones to the right are in frequency space. The two in the top are the initial settings, the ones in the middle show the overlap state, and the ones in the bottom represent the field configuration after the collision.

Sim. Box	Size	$80\mu\text{m}\times 80\mu\text{m}$
Background Pulse	$\vec{E}_0$	$(0, 0, 50) \text{ m}E_{cr}$
	$\hat{k}$	$(1, 0, 0)$
	$\vec{x}_0$	$(40, 40, 0) \mu\text{mm}$
	$w_0$	$4.6 \mu\text{m}$
	$z_r$	$16.619 \mu\text{m}$
	$\lambda$	$4 \mu\text{m}$
	$z_t$	$20 \mu\text{m}$
	$t$	$4.5 \mu\text{m}$
Probe Pulse	$\vec{E}_0$	$(0, 0, 50) \text{ m}E_{cr}$
	$\hat{k}$	$(-1, 0, 0)$
	***	<i>all other parameters as for the background</i>

Table 2: Parameters for the collision of two pulses with the same frequency in 2 dimensions. See figure 12 for results. Note that they are also the same for the orthogonal case except for the  $\hat{k}$ , which becomes  $(0, 1, 0)$

considered to be a point like photons, whereas here it they are considered to be a counter-propagating electromagnetic pulses. However, as seen in the discussion of the birefringence results in the present paper the flipping probability is mostly independent of pulse shape. It depends only on the frequency of the pulse and the relative angle between the polarizations of probe and background pulses. Due to this property of the interaction it is clear that the analytic calculations [14, 15] show such good agreement with the numerical approach in this paper.

Furthermore, while all analytical calculations in the literature consider only one effect at a time the simulations in this paper reproduce all of the effects simultaneously. Under certain conditions, a computation for a single effect is faster using the aforementioned analytical calculations. However, the simulated data represents the complete picture without having to consider how different effects interfere with each other. In addition, no restrictive assumptions need to be made about the initial setup. As a consequence numerical simulations can be used for real world experimental settings.

The properties of the algorithm in higher dimensions remain to be tested against predictions made for example in [16]. They will require a large number of expensive simulations to scan all the interesting parameters. Due to the fact that no specific assumptions concerning spatial directions have been made during the derivation of our numerical method we expect the algorithm to work in 3D.

Finally, as the number of assumptions that have been made in the course of the derivation of the numerical algorithm is small it is possible to use the latter to simulate all the predicted light by light scattering effects such as focusing or diffraction-angle specific polarization for a wide range of initial settings.

This in turn may be used to develop tomographic methods for strong pulse characterization.

## 10. Outlook

The ability to time resolve the nonlinear vacuum optical processes opens an array of interesting new investigations. For example, the intensity of the background pulse can be increased up to the point where the low energy approximation used to derive (45) no longer holds and the relative orthogonal polarization energy displays Rabi like oscillations [29]. An example of this ef-

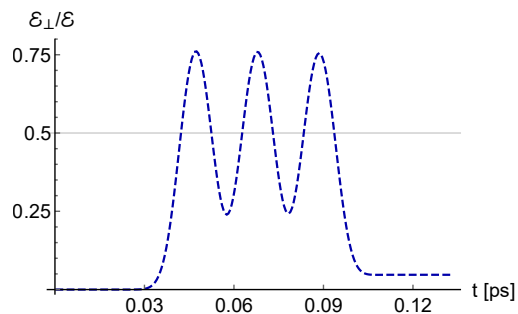


Figure 14: Plot of the time evolution of the relative perpendicular polarisation of the probe vs. time. The initial setup corresponds to the one shown in figure 9 [green line] with the exception of the amplitude of the background pulse being  $20 E_{cr}$ . The fact that the amplitude of the oscillations seen in the figure remains below 1 is due to the finite pulse width of the probe, which causes its different parts to have propagated through different amounts of the background at any given time.

fect can be seen in figure 14, where the intensity of the background has been increased to the ultra high field regime ( $20 E_{cr}$ ). The latter is only meant as a proof of the existence of Rabi-like oscillations under extreme conditions. However, the ultra-high field regime is at the limits of the validity range of the weak-field approximation of the HE-Lagrangian (4). It is also well past the point, where pair production (5) may be safely neglected. However, the effect is still worth considering as it may also be triggered by a longer weaker pulse.

## Acknowledgments

A.P.D. would like to acknowledge the support of P. Böhl during the familiarization period with the matter. This work was funded by the Munich Cluster of Excellence (MAP), by the international Max-Planck Research School for Advanced Photonic Sciences (IMPRS-APS), and the Transregio TR-18 project B12.

## References

## References

- [1] W. Heisenberg, H. Euler, Folgerungen aus der diracschen theorie des positrons, *Zeitschrift für Physik* 98 (11) 714–732. doi:10.1007/BF01343663.  
URL <http://dx.doi.org/10.1007/BF01343663>
- [2] J. Schwinger, On gauge invariance and vacuum polarization, *Phys. Rev.* 82 (1951) 664–679. doi:10.1103/PhysRev.82.664.  
URL <http://link.aps.org/doi/10.1103/PhysRev.82.664>
- [3] R. Baier, P. Breitenlohner, The vacuum refraction index in the presence of external fields, *Il Nuovo Cimento B Series* 10 47 (1) 117–120. doi: 10.1007/BF02712312.  
URL <http://dx.doi.org/10.1007/BF02712312>
- [4] D. Tommasini, H. Michinel, Light by light diffraction in vacuum, *Phys. Rev. A* 82 (2010) 011803. doi:10.1103/PhysRevA.82.011803.  
URL <http://link.aps.org/doi/10.1103/PhysRevA.82.011803>
- [5] Y. Monden, R. Kodama, Enhancement of laser interaction with vacuum for a large angular aperture, *Phys. Rev. Lett.* 107 (2011) 073602. doi: 10.1103/PhysRevLett.107.073602.  
URL <http://link.aps.org/doi/10.1103/PhysRevLett.107.073602>
- [6] B. King, C. H. Keitel, Photonphoton scattering in collisions of intense laser pulses, *New Journal of Physics* 14 (10) (2012) 103002.  
URL <http://stacks.iop.org/1367-2630/14/i=10/a=103002>
- [7] S. L. Adler, Photon splitting and photon dispersion in a strong magnetic field, *Annals of Physics* 67 (2) (1971) 599 – 647. doi:http://dx.doi.org/10.1016/0003-4916(71)90154-0.  
URL <http://www.sciencedirect.com/science/article/pii/0003491671901540>
- [8] H. Gies, F. Karbstein, N. Seegert, Quantum reflection as a new signature of quantum vacuum nonlinearity, *New Journal of Physics* 15 (8) (2013) 083002.  
URL <http://stacks.iop.org/1367-2630/15/i=8/a=083002>
- [9] B. King, P. Böhl, H. Ruhl, Interaction of photons traversing a slowly varying electromagnetic background, *Phys. Rev. D* 90 (2014) 065018. doi:10.1103/PhysRevD.90.065018.  
URL <http://link.aps.org/doi/10.1103/PhysRevD.90.065018>
- [10] P. Böhl, B. King, H. Ruhl, Vacuum high-harmonic generation in the shock regime, *Phys. Rev. A* 92 (2015) 032115. doi:10.1103/PhysRevA.92.032115.  
URL <http://link.aps.org/doi/10.1103/PhysRevA.92.032115>



- [11] C. Danson, D. Hillier, N. Hopps, D. Neely, Petawatt class lasers worldwide, *High Power Laser Science and Engineering* 3 (2015) e3 (14 pages). doi:10.1017/hpl.2014.52.  
URL [http://journals.cambridge.org/article\\_S2095471914000528](http://journals.cambridge.org/article_S2095471914000528)
- [12] T. Cowan, Hibef Collaboration, Status of the proposed Helmholtz International Beamline for Extreme Fields (HIBEF) at the European XFEL, in: *APS Meeting Abstracts*, 2013.
- [13] N. Miyanaga, H. Azechi, K. Tanaka, T. Kanabe, T. Jitsuno, J. Kawanaka, Y. Fujimoto, R. Kodama, H. Shiraga, K. Knodo, et al., 10-kj pw laser for the firex-i program, *Journal de Physique IV (Proceedings)* 133 (2006) 81–87.
- [14] F. Karbstein, H. Gies, M. Reuter, M. Zepf, Vacuum birefringence in strong inhomogeneous electromagnetic fields, *Phys. Rev. D* 92 (2015) 071301. doi:10.1103/PhysRevD.92.071301.  
URL <http://link.aps.org/doi/10.1103/PhysRevD.92.071301>
- [15] V. Dinu, T. Heinzl, A. Ilderton, M. Marklund, G. Torgrimsson, Vacuum refractive indices and helicity flip in strong-field qed, *Phys. Rev. D* 89 (2014) 125003. doi:10.1103/PhysRevD.89.125003.  
URL <http://link.aps.org/doi/10.1103/PhysRevD.89.125003>
- [16] V. Dinu, T. Heinzl, A. Ilderton, M. Marklund, G. Torgrimsson, Photon polarization in light-by-light scattering: Finite size effects, *Phys. Rev. D* 90 (2014) 045025. doi:10.1103/PhysRevD.90.045025.  
URL <http://link.aps.org/doi/10.1103/PhysRevD.90.045025>
- [17] H. Gies, L. Roessler, Vacuum polarization tensor in inhomogeneous magnetic fields, *Phys. Rev. D* 84 (2011) 065035. doi:10.1103/PhysRevD.84.065035.  
URL <http://link.aps.org/doi/10.1103/PhysRevD.84.065035>
- [18] G. V. Dunne, T. M. Hall, Borel summation of the derivative expansion and effective actions, *Phys. Rev. D* 60 (1999) 065002. doi:10.1103/PhysRevD.60.065002.  
URL <http://link.aps.org/doi/10.1103/PhysRevD.60.065002>
- [19] P. J. Mohr, D. B. Newell, B. N. Taylor, CODATA recommended values of the fundamental physical constants: 2014 (Jul 2015). [arXiv:1507.07956](https://arxiv.org/abs/1507.07956).
- [20] J. C. Maxwell, A dynamical theory of the electromagnetic field, *Philosophical Transactions of the Royal Society of London* 155 (1865) 459–512. doi:10.1098/rstl.1865.0008.  
URL <http://rstl.royalsocietypublishing.org/content/155/459.short>

- [21] W. H. Press, S. A. Teukolsky, W. T. Vetterling, B. P. Flannery, Numerical Recipes 3rd Edition: The Art of Scientific Computing, 3rd Edition, Cambridge University Press, 2007.
- [22] A. C. Hindmarsh, R. Serban, User documentation for ccode v2.8.2 (2015).  
URL [http://computation.llnl.gov/casc/sundials/documentation/cv\\_guide.pdf](http://computation.llnl.gov/casc/sundials/documentation/cv_guide.pdf)
- [23] W. R. Inc, Mathematica (2015).
- [24] A. Taflove, S. Hagness, Computational Electrodynamics: The Finite-difference Time-domain Method, Artech House antennas and propagation library, Artech House, 2005.  
URL <https://books.google.de/books?id=n2ViQgAACAAJ>
- [25] B. King, T. Heinzl, Measuring vacuum polarisation with high power lasers, arXiv preprint arXiv:1510.08456.
- [26] W. Dittrich, H. Gies, Probing the Quantum Vacuum: Perturbative Effective Action Approach in Quantum Electrodynamics and its Application, Springer Tracts in Modern Physics, Springer Berlin Heidelberg, 2003.  
URL <https://books.google.de/books?id=lctrCQAAQBAJ>
- [27] A. N. Luiten, J. C. Petersen, Detection of vacuum birefringence using intense laser pulses, Physics Letters A 330 (6) (2004) 429 – 434.  
doi:<http://dx.doi.org/10.1016/j.physleta.2004.08.020>.  
URL <http://www.sciencedirect.com/science/article/pii/S0375960104011442>
- [28] T. Heinzl, B. Liesfeld, K.-U. Amthor, H. Schworer, R. Sauerbrey, A. Wipf, On the observation of vacuum birefringence, Optics Communications 267 (2) (2006) 318 – 321. doi:<http://dx.doi.org/10.1016/j.optcom.2006.06.053>.  
URL <http://www.sciencedirect.com/science/article/pii/S0030401806006481>
- [29] D. Griffiths, Introduction to Electrodynamics, Prentice Hall, 1999.  
URL <https://books.google.de/books?id=M8XvAAAAMAAJ>